

Article

Metal-Organic Framework-Derived Atomically Dispersed Co-N-C Electrocatalyst for Efficient Oxygen Reduction Reaction

Dongqi Ge ^{1,2}, Longfei Liao ^{2,3,*}, Mingyu Li ³ and Yongli Yin ²¹ School of Chemical Engineering, Guangdong University of Petrochemical Technology, Maoming 525000, China² Space Science and Technology Institute (Shenzhen), Shenzhen 518117, China³ School of Materials Science and Engineering, Harbin Institute of Technology (Shenzhen), Shenzhen 518055, China

* Correspondence: liaolongfei123@126.com

Abstract: In this work, an atomically dispersed cobalt-nitrogen-carbon (Co-N-C) catalyst is prepared for the oxygen reduction reaction (ORR) by using a metal-organic framework (MOF) as a self-sacrifice template under high-temperature pyrolysis. Spherical aberration-corrected electron microscopy is employed to confirm the atomic dispersion of high-density Co atoms on the nitrogen-doped carbon scaffold. The X-ray photoelectron spectroscopy results verify the existence of Co-N-C active sites and their content changes with the Co content. The electrochemical results show that the electrocatalytic activity shows a volcano-shaped relationship, which increases with the Co content from 0 to 0.99 wt.% and then decreases when the presence of Co nanoparticles at 1.61 wt.%. The atomically dispersed Co-N-C catalyst with Co content of 0.99 wt.% shows an onset potential of 0.96 V vs. reversible hydrogen electrode (RHE) and a half-wave potential of 0.89 V vs. RHE toward ORR. The excellent ORR activity is attributed to the high density of the Co-N-C sites with high intrinsic activity and high specific surface area to expose more active sites.



Citation: Ge, D.; Liao, L.; Li, M.; Yin, Y. Metal-Organic Framework-Derived Atomically Dispersed Co-N-C Electrocatalyst for Efficient Oxygen Reduction Reaction.

Catalysts **2022**, *12*, 1462. <https://doi.org/10.3390/catal12111462>

Academic Editors: Dezhi Han, Wentai Wang and Ning Han

Received: 20 October 2022

Accepted: 16 November 2022

Published: 18 November 2022

Publisher's Note: MDPI stays neutral with regard to jurisdictional claims in published maps and institutional affiliations.



Copyright: © 2022 by the authors. Licensee MDPI, Basel, Switzerland. This article is an open access article distributed under the terms and conditions of the Creative Commons Attribution (CC BY) license (<https://creativecommons.org/licenses/by/4.0/>).

Keywords: metal-organic frameworks; cobalt-nitrogen-carbon; atomic dispersion; electrocatalysts; oxygen reduction reaction

1. Introduction

The oxygen reduction reaction (ORR) plays a significant role in energy conversion processes such as in fuel cells and metal-air batteries [1–3]. However, the sluggish kinetics of ORR result in a high overpotential, thus limiting the energy conversion efficiency of the system [4–6]. Pt-based electrocatalysts have been considered as the ideal material to boost the ORR; however, the high cost and source scarcity hamper their large-scale application [7–9]. Therefore, it is highly desirable to develop highly active and cost-effective alternative electrocatalysts to improve the electrocatalytic activity of the ORR.

In the past years, enormous efforts have been devoted to developing various Pt-free electrocatalysts for the ORR [10,11]. Among them, the nitrogen-coordinated transition-metal single-atom electrocatalysts (M-N-C SAC) have emerged as promising candidates due to their unique properties [12–15]. The M-N-C SAC with atomically isolated metal sites can avoid the aggregation behavior in metal nanoparticle electrocatalysts, thus enabling good stability and nearly 100% atomic utilization efficiency [16–18]. Moreover, the N atoms coordinated with metal sites can optimize the electronic structure of the M-N-C sites, which are regarded as the active sites of ORR [19]. In recent years, various M-N-C SACs have been prepared through high-temperature pyrolysis for the ORR, such as Fe-N-C SAC [20], Co-N-C SAC [21], and Cu-N-C SAC [22]. However, the metal ions tend to aggregate to form mixed structures of single-atom and nanoclusters or even nanoparticles under the direct treatment of metal salt precursors [23–25]. Therefore, the high dispersion of metal ions in the precursor is the key to achieving monoatomic dispersion. For example, the O, N-doped carbon supported W single atom catalyst was synthesized through the combination of a

metal-organic coordination polymer and pyrolysis strategy, in which the metal-organic coordination polymer enables the high dispersion of metal sites in the precursor [26]. The Fe-doped Zn-based MOFs were employed as the self-sacrifice templates to synthesize Fe-N-C SAC [27]. It is proposed that the Zn ions serve as the barriers to isolating the Fe atoms to avoid aggregation. Despite the significant progress, both the M-N-C SAC preparation and electrocatalytic activity investigation towards ORR are still insufficient.

In this work, various Co-N-C catalysts are prepared by using Co-doped Zn MOFs as self-sacrifice templates under high-temperature pyrolysis. The metal-organic frameworks (MOFs) with an ordered arrangement of metal ions and organic ligands enable the uniform distribution of metal ions in the framework [28–31], which exhibits great advantages in the preparation of atomically dispersed materials [32]. The high content of Zn ions enables the high dispersion of Co ions in the precursors and creates pores during evaporation. In addition, the nitrogen-containing organic ligands, 2,4,6-tris(4-pyridyl) triazine (TPT), can serve as carbon and nitrogen sources and create pores during decomposition. Moreover, melamine is mixed with Co-doped Zn MOFs as an extra nitrogen source to help the high-density assembly of Co-N-C sites. The physiochemical characterizations reveal that the Co-N-C catalysts with different Co contents exhibit various features. The optimized Co-N-C catalyst shows the atomic dispersion of Co atoms with a high density of Co-N-C sites and high specific surface area. The electrochemical results confirm that the atomically dispersed Co-N-C catalyst shows superior ORR activity in alkaline media than that of commercial Pt/C.

2. Results and Discussion

The atomically dispersed Co-N-C catalysts are synthesized by using Co-doped Zn-MOFs (Co-Zn-MOF) as self-sacrifice templates under high-temperature pyrolysis. First, the Co-Zn-MOF precursors are synthesized by dissolving various molar ratios of cobalt to zinc salts in the mixed solution of methanol and nitrobenzene with 2,4,6-tris(4-pyridyl) triazine (TPT) as a ligand. The obtained Zn-Co-MOFs refer to Co-Zn-MOF-1, Co-Zn-MOF-2, and Co-Zn-MOF-3 with the Co:Zn molar ratios of 1:19, 1:9, and 1:6.33, respectively. Second, the Co-Zn-MOFs mixed with melamine are pyrolyzed at 900 °C under an inert atmosphere to obtain the Co-N-C catalysts. For comparison, the nitrogen-doped carbon (N-C) catalyst is also synthesized with the mixture of melamine and Zn-MOF.

The morphologies of the Co-N-C catalysts are characterized by scanning electron microscopy (SEM). As shown in Figure 1a,b, the Co-Zn-MOF-1 exhibits polyhedral block morphologies as the Zn-MOF, while the Co-Zn-MOF-2 and Co-Zn-MOF-3 show aggregated irregular block morphologies due to the competition of Co^{2+} and Zn^{2+} coordinated with TPT, thus slowing down the nucleation rate of seeds (Figure 1c,d) [33]. X-ray diffraction (XRD) is employed to reveal the crystal structure of the obtained catalysts (Figure 1e). It is seen that the Co-Zn-MOF-1 shows nearly the same XRD pattern as the Zn-MOF, which indicates that the introduction of the low content of Co ions does not change the crystalline structure of Zn-MOF. However, the XRD patterns of Co-Zn-MOF-2 and Co-Zn-MOF-3 exhibit nearly the same XRD pattern as the Zn-MOF with the variation of diffraction peak intensity, which may be induced by larger Co ions doped into the Zn-MOF structure during the synthesis process.

The nanostructure of the as-obtained N-C and Co-N-C catalysts is characterized by SEM and transmission electron microscopy (TEM). It is seen from Figure S1 that all of the MOFs' structures are collapsed and show irregular porous structures after high-temperature treatment. As illustrated in Figure 2a–c, the N-C, Co-N-C-1, and Co-N-C-2 exhibit similar morphologies with wrinkles or curled edges in stacked sheets, and no obvious Co nanoparticles can be observed. When increasing the Co content, the Co nanoparticle appears in the Co-N-C-3 catalyst (Figure 2d). The XRD patterns of the Co-N-C catalysts further confirm the formation of the metallic Co phase in the Co-N-C-3 catalyst (Figure 2e). It is seen that the N-C, Co-N-C-1, and Co-N-C-2 only exhibit two diffraction peaks at 25.0° and 44.5°, which correspond to the (002) and (101) planes of carbon. The

diffraction peaks located at 44.2° , 51.5° , and 75.8° correspond to the (111), (200), and (220) planes of the cubic Co phase in Co-N-C-3 catalyst (PDF#15-0806), indicating the formation of Co nanoparticles when increasing the Co content. Based on the abovementioned SEM and XRD results, it is speculated that the Co single atoms are formed in Co-N-C-1 and Co-N-C-2 catalysts.

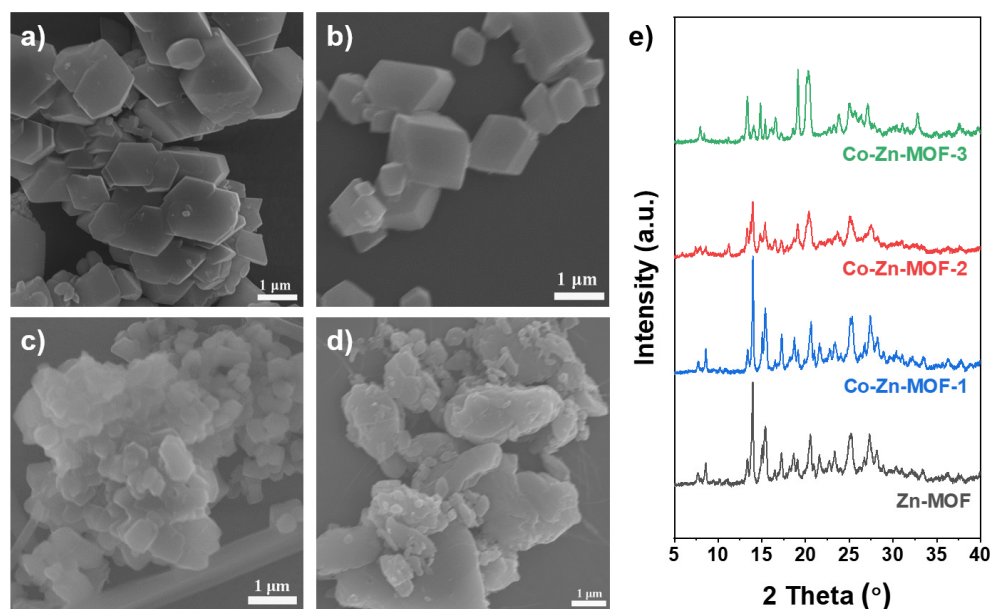


Figure 1. SEM images of (a) Zn-MOF, (b) Co-Zn-MOF-1, (c) Co-Zn-MOF-2, and (d) Co-Zn-MOF-3; (e) XRD patterns of the Zn-MOF and Co-Zn-MOF precursors.

To further confirm the suspect, high-angle annular dark-field scanning transmission electron microscopy (HAADF-STEM) is employed to characterize the nanostructure of Co in the Co-N-C-2 catalyst. The HAADF-STEM image exhibits some bright dots ascribing to the isolated Co atoms (Figure 2f), confirming the single-atom feature of the Co-N-C-2 catalyst (some of the bright dots are marked with yellow circles). Furthermore, the corresponding elemental mapping images reflect the homogeneous distribution of Co, C, N, and O on the surface of the Co-N-C-2 (Figure 2g). The abovementioned results demonstrate the successful synthesis of cobalt single-atom catalysts.

Nitrogen ad/desorption isotherms are employed to investigate the porous feature of the catalysts, as shown in Figure 3a. The typical type-IV isotherms at a relative pressure of ca. 0.5–1.0 with an H4 hysteresis loop indicate a micro-mesoporous porous structure [34], which is created by the released gases of organic precursors' decomposition and Zn evaporation at high temperature. It is seen that the specific surface area of the catalyst is composed of the micropore area and mesopore area, of which the micropore area is the dominant area. The dominant micropore area corresponds to the micropore feature of MOF, while the mesopore area may be attributed to the decomposition of the organic ligand. The pore size distribution also confirms the micro-mesopore feature of the Co-N-C catalysts (Figure S3). The specific surface area of the catalysts is first gradually increased by increasing the Co content, and then shows a slight decrease when the nanoparticle appears, which follows the order of N-C ($840 \text{ m}^2 \text{ g}^{-1}$) < Co-N-C-1 ($880 \text{ m}^2 \text{ g}^{-1}$) < Co-N-C-3 ($1003 \text{ m}^2 \text{ g}^{-1}$) < Co-N-C-2 ($1076 \text{ m}^2 \text{ g}^{-1}$) (Figure 3b and Table S1). The increased specific surface area may be attributed to the coordination of Co with the carbon precursor during the pyrolysis, thus affecting the decomposition of organic precursors.

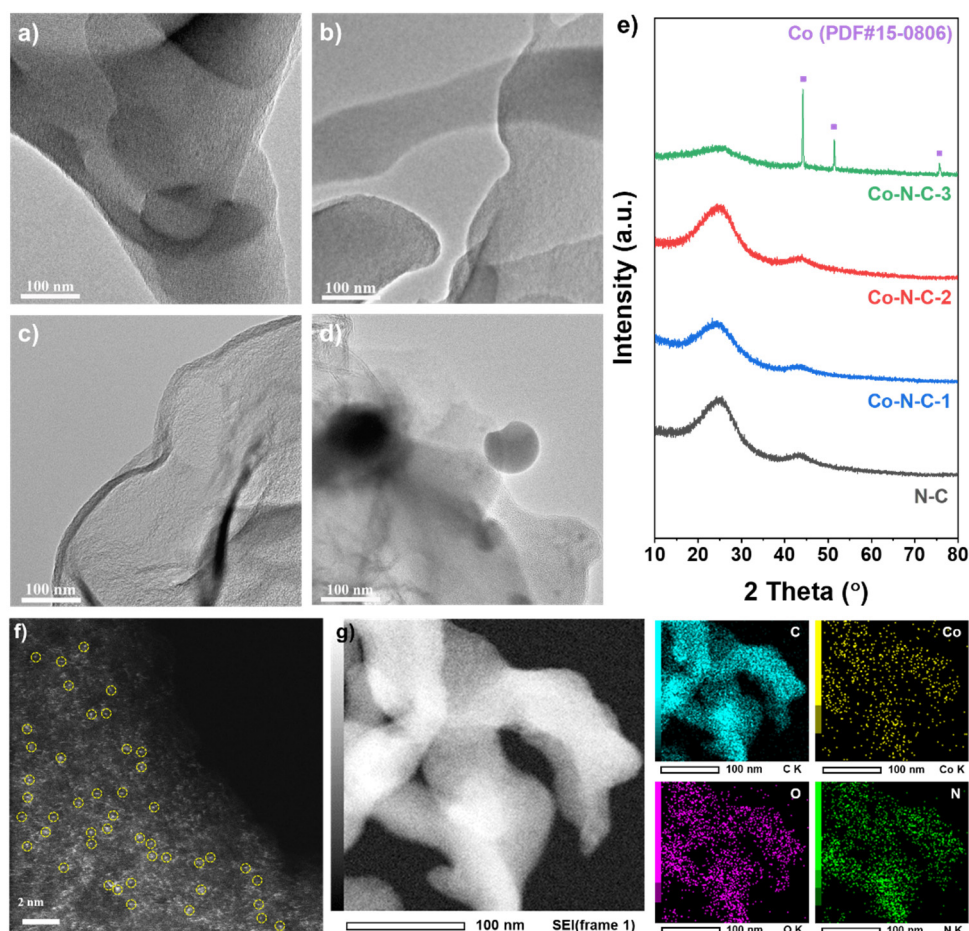


Figure 2. TEM images of (a) N-C, (b) Co-N-C-1, (c) Co-N-C-2, and (d) Co-N-C-3; (e) XRD patterns of the N-C and Co-N-C catalysts; (f) HAADF-STEM image of Co-N-C-2 catalyst (some of the bright dots are marked with yellow circles) and (g) the corresponding elemental mapping images.

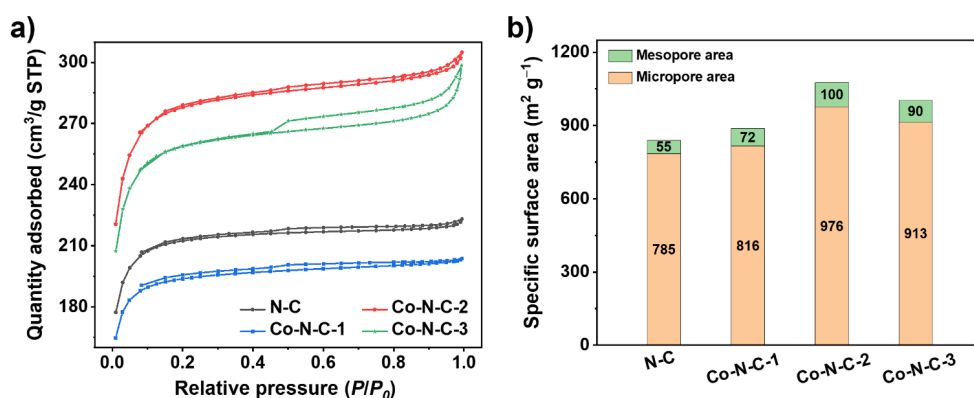


Figure 3. (a) Nitrogen adsorption–desorption isotherms of the N-C and Co-N-C catalysts; (b) specific surface areas of the N-C and Co-N-C catalysts.

The surface elemental compositions of N-C and Co-N-C catalysts are investigated by X-ray photoelectron spectroscopy (XPS). The full XPS spectra show that C, N, and O are present in N-C and Co-N-C catalysts (Figure 4a). It is worth noting that no obvious Co peaks can be observed from the survey spectra due to their low contents, and the signal of Co peaks can be observed from the high-resolution Co 2p spectra. It is seen that the intensity of the Co peaks is increased by increasing the Co content, as shown in Figure 4b, and the elemental contents are listed in Table S2. The Co content is gradually increased

from 0.66 to 1.61 wt.%, and the nanoparticles are formed at the content of 1.61 wt.%. The isolating effect of Zn is decreased at a higher Co content, and the closed Co atoms prefer to form metallic Co nanoparticles at temperature. The high-resolution Co 2p peaks are deconvoluted to four sub-peaks, corresponding to Co 2p_{1/2} (795.5 eV), Co 2p_{3/2} (780.5 eV), and two characteristic satellite peaks (802.7, and 787.7 eV) (Figure 4c and Figure S3) [35,36]. The Co 2p_{1/2} and Co 2p_{3/2} represent the oxidation states of Co, which may be attributed to the coordination of Co with N, as well as the oxidation when exposed to the air. The N contents of the catalysts are first gradually increased by increasing Co content, and then show a decrease when the nanoparticles appear (Table S2). The increased N content may be assigned to the coordination of Co with N, thus maintaining more N species in the obtained material. The decrease in the N content of Co-N-C-3 can be attributed to the decreased amount of Co coordinated with N after the formation of Co nanoparticles. The high-resolution N 1s peaks of the Co-N-C catalysts are also deconvoluted to four sub-peaks, corresponding to pyridinic-N (\approx 398.4 eV), Co-N (\approx 399.2 eV), graphitic-N (\approx 401 eV) and oxidized-N (\approx 403 eV), as shown in Figure 4d and Figure S4 [37,38]. The content of each nitrogen component of these catalysts is summarized in Table S3. The Co-N content is first increased by increasing the Co content, and then decreased when Co nanoparticles appear in the Co-N-C-3 catalyst. This is because the Co nanoparticles are wrapped into the Co-N-C-3, causing the diminishment of Co-N sites on the surface [39]. Among these catalysts, the Co-N-C-2 shows the highest Co-N content, as well as the highest N content. It is reported that Co coordinates with N can result in a regulated electronic structure, which will benefit the adsorption of oxygen species during ORR. It is expected that the ORR activity follows the above trends.

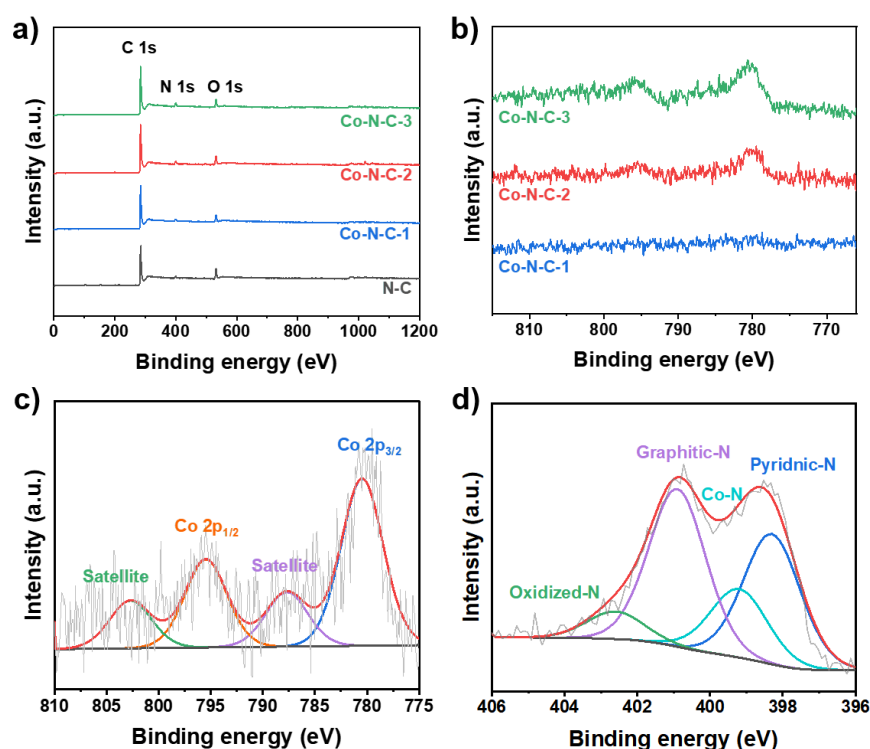


Figure 4. (a) XPS survey spectra of the N-C and Co-N-C catalysts; (b) Co 2p spectra of the Co-N-C catalysts; (c) Co 2p peaks and the fitting result of the Co-N-C-2; (d) N 1s peaks and the fitting result of the Co-N-C-2.

Upon the investigation of the structure and composition of as-prepared catalysts, cyclic voltammetry (CV) and linear sweep voltammetry (LSV) are implemented to explore their electrochemical performance. It is seen from Figure 5a that the CV curves of N-C and Co-N-C catalysts exhibit electrochemical double-layer capacitances without obvious

redox coupling of cobalt species, manifesting that there are no metal nanoparticles on the surface. The capacitance current shows a volcano-shaped relationship, which first increases and then dramatically decreases in the presence of the Co nanoparticles. It is seen that the electrochemical double-layer capacitances are related to the specific surface area. The polarization curves of the ORR are collected in an O₂-saturated 0.1 M KOH solution, as shown in Figure 5b. It is seen that all of the Co-N-C catalysts exhibit higher ORR activities than the N-C and commercial Pt/C catalysts due to the high intrinsic ORR activity of the Co-N-C sites. The electrocatalytic performance shows a volcano-shaped relationship, which increases with the Co content from 0 to 0.99 wt.% and then decreases at 1.61 wt.%. The Co-N-C-2 shows the highest ORR activity with an onset potential (E_{onset}) of 0.96 V vs. RHE and a half-wave potential ($E_{1/2}$) of 0.89 V vs. RHE, which makes it one of the best-performing catalysts for OER reported in the literature (Figure 5c and Table S4). Moreover, the Co-N-C-2 catalyst shows a nearly four-electron transfer process with a low yield of hydrogen peroxide (Figure S5). Combining the above physicochemical characterizations, it can be concluded that the outstanding electrocatalytic activity should be attributed to the high density of Co-N sites with high intrinsic activity and high specific surface area with improved exposure of the active site.

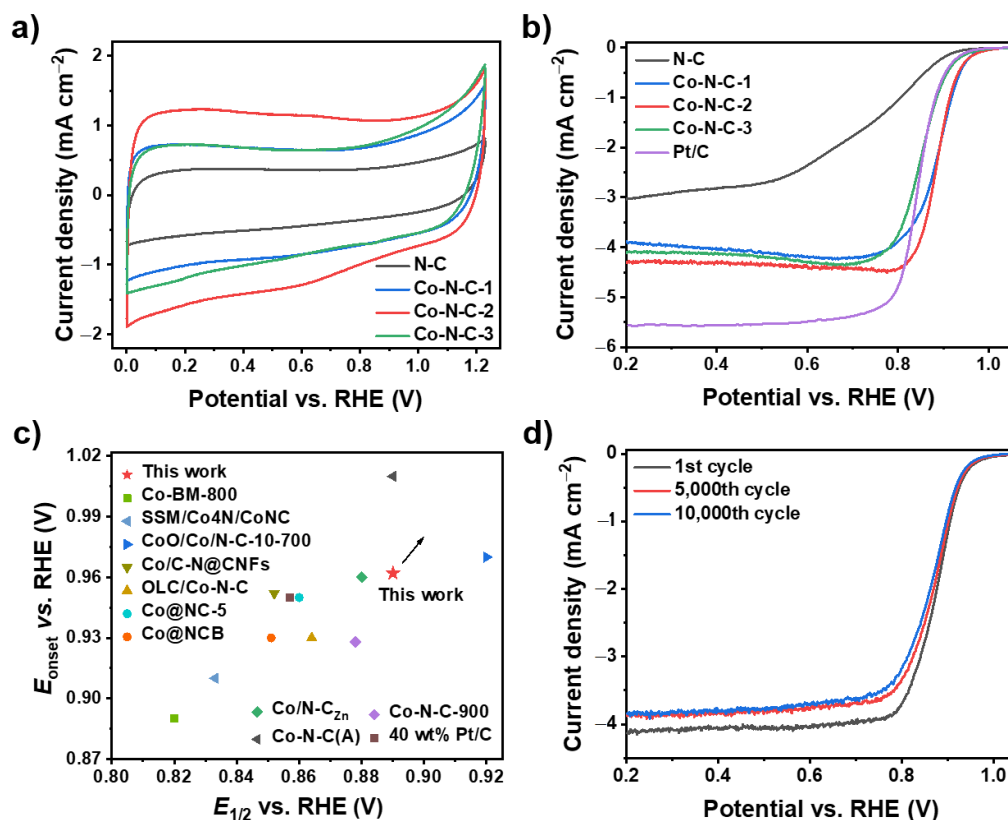


Figure 5. (a) CV curves of the catalysts in N₂-saturated 0.10 M KOH; (b) ORR polarization curves of the catalysts in O₂-saturated 0.10 M KOH; (c) comparison of the E_{onset} and $E_{1/2}$ of the Co-N-C-2 towards ORR with the previously reported catalysts [35,38,40–47]; (d) ORR polarization curves of Co-N-C-2 catalyst after different potential cycles in O₂-saturated 0.10 M KOH.

Finally, the stability of the Co-N-C-2 catalyst is evaluated with the accelerated degradation test (ADT) by cycling the catalyst in O₂-saturated 0.1 M KOH at 100 mV s⁻¹ in the potential range of 0.6–1.0 V vs. RHE. The LSV curves show that the $E_{1/2}$ of the Co-N-C-2 catalyst only decreased 9 mV after 10,000 potential cycles, indicating its excellent stability (Figure 5d).

3. Materials and Methods

3.1. Material Synthesis

Synthesis of TPT: The TPT was prepared as per the previous report [48]. Typically, 288 mmol 4-cyanopyridine was put into the flask and heated to 150 °C to melt, and 28.8 mmol NaOH was added into the flask and stirred at 150 °C for 24 h. The obtained solid was washed with acetone and dissolved in hydrochloric acid. Then, the active carbon was added to the solution and sonicated for 30 min. The suspension was filtered and neutralized with NaOH. Finally, the product was filtered, washed with water and acetone, and dried under vacuum at 60 °C overnight.

Synthesis of Zn-MOF and Co-Zn-MOFs: The Zn-MOF of $(\text{ZnBr}_2)_3(\text{TPT})_2$ was prepared as per the previous report [49]. Typically, 1.60 mmol 2,4,6-Tris(4-pyridyl)-1,3,5-triazine (TPT) was dissolved into the mixed solution of nitrobenzene/methanol (320/40 mL). Then, an 80 mL methanol solution with 2.40 mmol ZnBr_2 was added to the TPT solution and stirred vigorously for 5 min. The obtained white power was filtered, washed with ethyl alcohol, and dried under vacuum at 60 °C overnight. The Zn-Co-MOFs were prepared using the same procedure as Zn-MOF except for the partial replacement of ZnBr_2 with $\text{CoCl}_2 \cdot 6\text{H}_2\text{O}$. The obtained Zn-Co-MOFs were denoted to Co-Zn-MOF-1, Co-Zn-MOF-2, and Co-Zn-MOF-3 with the Co:Zn molar ratios of 1:19, 1:9, and 1:6.33, respectively.

Synthesis of N-C and Co-N-C catalysts: First, 500 mg of Zn-MOF or Zn-Co-MOFs and 40 mg melamine were mixed and transferred into a quartz boat. Second, the above mixture was pyrolyzed at 900 °C for 1 h with a heating rate of 10 °C min^{-1} under the argon atmosphere (99.999%) to obtain the catalysts. The catalyst derived from Zn-MOF, Co-Zn-MOF-1, Co-Zn-MOF-2, and Co-Zn-MOF-3 were denoted to N-C, Co-N-C-1, Co-N-C-2, and Co-N-C-3, respectively.

3.2. Physicochemical Characterizations

Powder X-ray diffraction (PXRD) patterns were collected on a Rigaku MiniFlex600 (Rigaku, Tokyo, Japan) with $\text{Cu K}\alpha$ radiation ($\lambda = 1.54178 \text{ \AA}$). Scanning electron microscopy (SEM), as well as corresponding elemental mapping and energy-dispersive X-ray spectroscopy (EDX) analysis, were carried out on a Hitachi SU 8220 (Hitachi, Ibaraki, Japan). Transmission electron microscopy (TEM) was carried out on a JEOL JEM-2100 (JEOL, Tokyo, Japan). The HAADF-STEM and mapping images were taken using a JEOL JEM-ARM300F with an operating voltage of 300 kV. X-ray photoelectron spectroscopy (XPS) experiments were carried out on Thermo Scientific K-Alpha (Thermo Fisher Scientific, Waltham, MA, USA). The pore structure of the samples was probed by nitrogen adsorption/desorption isotherms at 77 K (Micromeritics ASAP 2020, Micromeritics, Norcross, GA, USA). Before the measurements, the samples were outgassed at 100 °C for 12 h. The specific surface area was calculated with the Brunauer-Emmett-Teller (BET) model and the pore size distribution was obtained by desorption branches of isotherms using the Barrett-Joyner-Halenda (BJH) method.

3.3. Electrochemical Measurements

Cyclic voltammetry (CV) and linear sweep voltammetry (LSV) were conducted by CHI 730E (CH Instruments, Inc., Austin, TX, USA) at room temperature with a three-electrode system. A rotating disk electrode (RDE) with 5 mm diameter glassy carbon was used as the working electrode, which was coated with the electrocatalyst. The working electrode was prepared as follows: 5 mg of electrocatalyst was dispersed in 500 μL of Nafion/ethanol (0.84 wt.% Nafion) by ultrasonication for 60 min to obtain a homogeneous ink; then 10 μL catalyst ink was drop-cast onto the RDE. For comparison, the ORR electrocatalytic activity of commercial 40 wt.% Pt/C (HiSPEC4000, Johnson Matthey, London, UK) was also evaluated with the Pt loading of 20 $\mu\text{g cm}^{-2}$. The test result potentials were converted to the reversible hydrogen electrode (RHE) using the following formula: $E_{\text{RHE}} = E_{\text{SCE}} + 0.0591\text{pH}$.

The CV curves were recorded at 20 mV s^{-1} in the potential range from 0 to 1.23 V (vs. RHE) in an N_2 -saturated 0.10 M KOH solution. The LSV curves were measured at

5 mV s⁻¹ in O₂-saturated 0.10 M KOH at a rotating speed of 1600 rpm. The accelerated durability tests (ADTs) were conducted by continuous CV tests between 0.60 and 1.00 V (vs. RHE) with the rate of 100 mV s⁻¹ in O₂-saturated 0.10 M KOH solution. The LSV test was carried out after 5000 cycles and 10,000 cycles.

The electron-transfer number (n) was tested on a rotating ring-disk electrode (RRDE, glassy carbon disk: 5.0 mm in diameter; platinum ring: 6.5 mm inner diameter and 7.5 mm outer diameter) electrode. The electron-transfer number (n) and hydrogen peroxide yield (H₂O₂%) in the ORR were calculated from the following equations:

$$n = \frac{4|i_d|}{|i_d| + i_r/N}$$
$$\text{H}_2\text{O}_2(\%) = \frac{2i_r/N}{|i_d| + i_r/N} \times 10$$

where i_d is the disk current, i_r is the ring current, and N is the collection efficiency.

4. Conclusions

An atomically dispersed Co-N-C catalyst was developed for the ORR with a Co-doped Zn-MOF precursor as the self-sacrifice template. The Zn-MOF with an ordered arrangement of metal ions resulted in a high dispersion of Co atoms with a porous structure, while the organic ligand of 4,6-tris(4-pyridyl) triazine resulted in a nitrogen-doped carbon with a high specific surface area. The extra nitrogen source of melamine facilitated the high-density assembly of Co-N-C sites. The atomically dispersed Co-N-C catalysts formed at low Co contents, which aggregated to form Co nanoparticles at a Co content of 1.61 wt.%. The optimized atomically dispersed Co-N-C catalyst with a high density of Co-N sites and a high specific surface area thus facilitates the ORR. The atomically dispersed Co-N-C catalyst with a Co content of 0.99 wt.% shows an E_{onset} of 0.96 V vs. RHE and an $E_{1/2}$ of 0.89 V vs. RHE toward ORR. This work provides a general strategy to develop atomically dispersed metal-based catalysts for electrocatalysis.

Supplementary Materials: The following supporting information can be downloaded at: <https://www.mdpi.com/article/10.3390/catal12111462/s1>, XPS analysis; Figure S1: SEM images of (a) N-C, (b) Co-N-C-1, (c) Co-N-C-2, and (d) Co-N-C-3; Figure S2: HAADF-STEM images of the Co-N-C-2 catalyst; Figure S3: The pore size distribution of the obtained NC and Co-N-C catalysts; Figure S4: Co 2p peaks and fitting results of (a) Co-N-C-1, and (b) Co-N-C-3; Figure S5: N 1s peaks and fitting results of (a) N-C, (b) Co-N-C-1, and (c) Co-N-C-3; Figure S6: The yield of hydrogen peroxide (%) and electron transfer number of the Co-N-C-2 catalyst toward ORR; Table S1. Pore features of the N-C and Co-N-C catalysts; Table S2. Surface elemental composition (wt.%) of the obtained materials measured by XPS; Table S3. Content of each nitrogen component (%) of the N-C and Co-N-C catalysts; Table S4. Comparison of the ORR catalytic performance of the Co-N-C-2 SACs catalyst and the other M-N-C catalysts reported in the literature in 0.1 M KOH. References [35,36,38,40–47,50–58] are cited in Supplementary Materials.

Author Contributions: Conceptualization, D.G. and L.L.; methodology and writing—original draft preparation, D.G. and L.L.; writing—review and editing, D.G., L.L., M.L. and Y.Y.; supervision, L.L., M.L. and Y.Y. All authors have read and agreed to the published version of the manuscript.

Funding: This research was funded by the Foundation of the National Key Laboratory of Human Factors Engineering, China Astronaut, Research and Training Center (grant number: 6142222210601).

Data Availability Statement: Not applicable.

Acknowledgments: Thanks for the support of physicochemical characterizations from Harbin Institute of Technology (Shenzhen).

Conflicts of Interest: The authors declare no conflict of interest.

References

1. Hutchison, P.; Rice, P.S.; Warburton, R.E.; Raugei, S.; Hammes-Schiffer, S. Multilevel Computational Studies Reveal the Importance of Axial Ligand for Oxygen Reduction Reaction on Fe-N-C Materials. *J. Am. Chem. Soc.* **2022**, *144*, 16524–16534. [[CrossRef](#)] [[PubMed](#)]
2. Zhao, X.; Yu, X.; Xin, S.; Chen, S.; Bao, C.; Xu, W.; Xue, J.; Hui, B.; Zhang, J.; She, X.; et al. Enhanced Oxygen Reduction Reaction for Zn-Air Battery At Defective Carbon Fibers Derived From Seaweed Polysaccharide. *Appl. Catal. B Environ.* **2022**, *301*, 120785. [[CrossRef](#)]
3. Xie, X.Y.; Shang, L.; Xiong, X.Y.; Shi, R.; Zhang, T.R. Fe Single-Atom Catalysts on MOF-5 Derived Carbon for Efficient Oxygen Reduction Reaction in Proton Exchange Membrane Fuel Cells. *Adv. Energy Mater.* **2022**, *12*, 2102688. [[CrossRef](#)]
4. Han, N.; Feng, S.; Guo, W.; Mora, O.M.; Zhao, X.; Zhang, W.; Xie, S.; Zhou, Z.; Liu, Z.; Liu, Q.; et al. Rational Design of Ruddlesden–Popper Perovskite Electrocatalyst for Oxygen Reduction to Hydrogen Peroxide. *SusMat* **2022**, *2*, 456–465. [[CrossRef](#)]
5. Ruan, M.B.; Liu, J.; Song, P.; Xu, W.L. Meta-Analysis of Commercial Pt/C Measurements for Oxygen Reduction Reactions via Data Mining. *Chin. J. Catal.* **2022**, *43*, 116–121. [[CrossRef](#)]
6. Lim, J.; Jung, C.; Hong, D.; Bak, J.; Shin, J.; Kim, M.; Song, D.; Lee, C.; Lim, J.; Lee, H.; et al. Atomically Ordered Pt₃Mn Intermetallic Electrocatalysts for the Oxygen Reduction Reaction in Fuel Cells. *J. Mater. Chem. A* **2022**, *10*, 7399–7408. [[CrossRef](#)]
7. Huang, S.Y.; Shan, A.X.; Wang, R.M. Low Pt Alloyed Nanostructures for Fuel Cells Catalysts. *Catalysts* **2018**, *8*, 538. [[CrossRef](#)]
8. Peng, J.H.; Tao, P.; Song, C.Y.; Shang, W.; Deng, T.; Wu, J.B. Structural Evolution of Pt-based Oxygen Reduction Reaction Electrocatalysts. *Chin. J. Catal.* **2022**, *43*, 47–58. [[CrossRef](#)]
9. Costa de Oliveira, M.A.; D’Epifanio, A.; Ohnuki, H.; Mecheri, B. Platinum Group Metal-Free Catalysts for Oxygen Reduction Reaction: Applications in Microbial Fuel Cells. *Catalysts* **2020**, *10*, 475. [[CrossRef](#)]
10. Luo, E.; Chu, Y.; Liu, J.; Shi, Z.; Zhu, S.; Gong, L.; Ge, J.; Choi, C.H.; Liu, C.; Xing, W. Pyrolyzed M-N_x Catalysts for Oxygen Reduction Reaction: Progress and Prospects. *Energ. Environ. Sci.* **2021**, *14*, 2158–2185. [[CrossRef](#)]
11. Cruz-Martinez, H.; Guerra-Cabrera, W.; Flores-Rojas, E.; Ruiz-Villalobos, D.; Rojas-Chavez, H.; Pena-Castaneda, Y.A.; Medina, D.I. Pt-Free Metal Nanocatalysts for the Oxygen Reduction Reaction Combining Experiment and Theory: An Overview. *Molecules* **2021**, *26*, 6689. [[CrossRef](#)] [[PubMed](#)]
12. Zhang, J.C.; Yang, H.B.; Liu, B. Coordination Engineering of Single-Atom Catalysts for the Oxygen Reduction Reaction: A Review. *Adv. Energy Mater.* **2021**, *11*, 2002473. [[CrossRef](#)]
13. Cepitis, R.; Kongi, N.; Grozovski, V.; Ivanistsev, V.; Lust, E. Multifunctional Electrocatalysis on Single-Site Metal Catalysts: A Computational Perspective. *Catalysts* **2021**, *11*, 1165. [[CrossRef](#)]
14. Shen, S.Q.; Sun, Y.Y.; Sun, H.; Pang, Y.P.; Xia, S.X.; Chen, T.Q.; Zheng, S.Y.; Yuan, T. Research Progress in ZIF-8 Derived Single Atomic Catalysts for Oxygen Reduction Reaction. *Catalysts* **2022**, *12*, 525. [[CrossRef](#)]
15. Lv, H.W.; Guo, W.X.; Chen, M.; Zhou, H.; Wu, Y. Rational Construction of Thermally Stable Single Atom Catalysts: From Atomic Structure to Practical Applications. *Chin. J. Catal.* **2022**, *43*, 71–91. [[CrossRef](#)]
16. Wang, Y.; Wang, D.; Li, Y. Atom-Level Interfacial Synergy of Single-Atom Site Catalysts for Electrocatalysis. *J. Energy Chem.* **2022**, *65*, 103–115. [[CrossRef](#)]
17. Wang, Y.; Su, H.; He, Y.; Li, L.; Zhu, S.; Shen, H.; Xie, P.; Fu, X.; Zhou, G.; Feng, C.; et al. Advanced Electrocatalysts with Single-Metal-Atom Active Sites. *Chem. Rev.* **2020**, *120*, 12217–12314. [[CrossRef](#)]
18. He, Y.; Liu, S.; Priest, C.; Shi, Q.; Wu, G. Atomically Dispersed Metal-Nitrogen-Carbon Catalysts for Fuel Cells: Advances in Catalyst Design, Electrode Performance, and Durability Improvement. *Chem. Soc. Rev.* **2020**, *49*, 3484–3524. [[CrossRef](#)]
19. Gao, C.; Mu, S.; Yan, R.; Chen, F.; Ma, T.; Cao, S.; Li, S.; Ma, L.; Wang, Y.; Cheng, C. Recent Advances in ZIF-Derived Atomic Metal-N-C Electrocatalysts for Oxygen Reduction Reaction: Synthetic Strategies, Active Centers, and Stabilities. *Small* **2022**, *18*, 2105409. [[CrossRef](#)]
20. Li, J.C.; Maurya, S.; Kim, Y.S.; Li, T.; Wang, L.G.; Shi, Q.R.; Liu, D.; Feng, S.; Lin, Y.H.; Shao, M.H. Stabilizing Single-Atom Iron Electrocatalysts for Oxygen Reduction via Ceria Confining and Trapping. *ACS Catal.* **2020**, *10*, 2452–2458. [[CrossRef](#)]
21. Cheng, Y.J.; Song, H.Q.; Yu, J.K.; Chang, J.W.; Waterhouse, G.I.N.; Tang, Z.Y.; Yang, B.; Lu, S.Y. Carbon Dots-Derived Carbon Nanoflowers Decorated with Cobalt Single Atoms and Nanoparticles as Efficient Electrocatalysts for Oxygen Reduction. *Chin. J. Catal.* **2022**, *43*, 2443–2452. [[CrossRef](#)]
22. Yang, L.; Xu, H.; Liu, H.; Zeng, X.; Cheng, D.; Huang, Y.; Zheng, L.; Cao, R.; Cao, D. Oxygen-Reconstituted Active Species of Single-Atom Cu Catalysts for Oxygen Reduction Reaction. *Research* **2020**, *2020*, 7593023. [[CrossRef](#)] [[PubMed](#)]
23. Ji, J.P.; Zhang, Y.P.; Tang, L.B.; Liu, C.Y.; Gao, X.H.; Sun, M.H.; Zheng, J.C.; Ling, M.; Liang, C.D.; Lin, Z. Platinum Single-Atom and Cluster Anchored on Functionalized MWCNTs with Ultrahigh Mass Efficiency for Electrocatalytic Hydrogen Evolution. *Nano Energy* **2019**, *63*, 103849. [[CrossRef](#)]
24. Xu, D.; Wang, S.; Wu, B.; Zhang, B.; Qin, Y.; Huo, C.; Huang, L.; Wen, X.; Yang, Y.; Li, Y. Highly Dispersed Single-Atom Pt and Pt Clusters in the Fe-Modified KL Zeolite with Enhanced Selectivity for n-Heptane Aromatization. *ACS Appl. Mater. Interfaces* **2019**, *11*, 29858–29867. [[CrossRef](#)]
25. Hu, C.; Song, E.; Wang, M.; Chen, W.; Huang, F.; Feng, Z.; Liu, J.; Wang, J. Partial-Single-Atom, Partial-Nanoparticle Composites Enhance Water Dissociation for Hydrogen Evolution. *Adv. Sci.* **2021**, *8*, 2001881. [[CrossRef](#)]

26. Zhang, F.; Zhu, Y.; Tang, C.; Chen, Y.; Qian, B.; Hu, Z.; Chang, Y.C.; Pao, C.W.; Lin, Q.; Kazemi, S.A.; et al. High-Efficiency Electrosynthesis of Hydrogen Peroxide from Oxygen Reduction Enabled by a Tungsten Single Atom Catalyst with Unique Terdentate N1O2 Coordination. *Adv. Funct. Mater.* **2021**, *32*, 2110224. [[CrossRef](#)]
27. Zhang, H.G.; Chung, H.T.; Cullen, D.A.; Wagner, S.; Kramm, U.I.; More, K.L.; Zelenay, P.; Wu, G. High-Performance Fuel Cell Cathodes Exclusively Containing Atomically Dispersed Iron Active Sites. *Energ. Environ. Sci.* **2019**, *12*, 2548–2558. [[CrossRef](#)]
28. Alshorifi, F.T.; Tobbala, D.E.; El-Bahy, S.M.; Nassan, M.A.; Salama, R.S. The Role of Phosphotungstic Acid in Enhancing the Catalytic Performance of UiO-66 (Zr) and its Applications as an Efficient Solid Acid Catalyst for Coumarins and Dihydropyrimidinones Synthesis. *Catal. Commun.* **2022**, *169*, 106479. [[CrossRef](#)]
29. Altass, H.M.; Ahmed, S.A.; Salama, R.S.; Moussa, Z.; Jassas, R.S.; Alsantali, R.I.; Al-Rooqi, M.M.; Ibrahim, A.A.; Khder, M.A.; Morad, M.; et al. Low Temperature CO Oxidation Over Highly Active Gold Nanoparticles Supported on Reduced Graphene Oxide@Mg-BTC Nanocomposite. *Catal. Lett.* **2022**. [[CrossRef](#)]
30. Al-Thabaiti, S.A.; Mostafa, M.M.M.; Ahmed, A.I.; Salama, R.S. Synthesis of Copper/Chromium Metal Organic Frameworks—Derivatives as an Advanced Electrode Material for High-Performance Supercapacitors. *Ceram. Int.* **2022**, *in press*. [[CrossRef](#)]
31. Li, Z.Q.; Gao, R.; Feng, M.; Deng, Y.P.; Xiao, D.J.; Zheng, Y.; Zhao, Z.; Luo, D.; Liu, Y.L.; Zhang, Z.; et al. Modulating Metal-Organic Frameworks as Advanced Oxygen Electrocatalysts. *Adv. Energy Mater.* **2021**, *11*, 2003291. [[CrossRef](#)]
32. Song, Z.X.; Zhang, L.; Doyle-Davis, K.; Fu, X.Z.; Luo, J.L.; Sun, X.L. Recent Advances in MOF-Derived Single Atom Catalysts for Electrochemical Applications. *Adv. Energy Mater.* **2020**, *10*, 2001561. [[CrossRef](#)]
33. Sun, W.; Du, L.; Tan, Q.; Zhou, J.; Hu, Y.; Du, C.; Gao, Y.; Yin, G. Engineering of Nitrogen Coordinated Single Cobalt Atom Moieties for Oxygen Electroreduction. *ACS Appl. Mater. Interfaces* **2019**, *11*, 41258–41266. [[CrossRef](#)] [[PubMed](#)]
34. Thommes, M.; Kaneko, K.; Neimark, A.V.; Olivier, J.P.; Rodriguez-Reinoso, F.; Rouquerol, J.; Sing, K.S.W. Physisorption Of Gases, with Special Reference to the Evaluation of Surface Area and Pore Size Distribution (IUPAC Technical Report). *Pure Appl. Chem.* **2015**, *87*, 1051–1069. [[CrossRef](#)]
35. Meng, H.; Liu, Y.; Liu, H.; Pei, S.; Yuan, X.; Li, H.; Zhang, Y. ZIF67@MFC-Derived Co/N-C@CNFs Interconnected Frameworks with Graphitic Carbon-Encapsulated Co Nanoparticles as Highly Stable and Efficient Electrocatalysts for Oxygen Reduction Reactions. *ACS Appl. Mater. Interfaces* **2020**, *12*, 41580–41589. [[CrossRef](#)]
36. Zhao, S.L.; Yang, J.; Han, M.; Wang, X.M.; Lin, Y.; Yang, R.; Xu, D.D.; Shi, N.E.; Wang, Q.; Yang, M.J.; et al. Synergistically Enhanced Oxygen Reduction Electrocatalysis by Atomically Dispersed and Nanoscaled Co Species in Three-Dimensional Mesoporous Co, N-codoped Carbon Nanosheets Network. *Appl. Catal. B Environ.* **2020**, *260*, 118207. [[CrossRef](#)]
37. Yue, C.; Zhang, N.; Zhu, Z.; Chen, P.; Meng, F.; Liu, X.; Wei, X.; Liu, J. Multi-Strategy Architecture of High-Efficiency Electrocatalysts for Underwater Zn-H₂O₂ Batteries with Superior Power Density of 442 mW cm⁻². *Small* **2022**, *18*, 2106532. [[CrossRef](#)]
38. Zhang, D.; Sun, P.P.; Zhou, Q.; Li, B.; Wei, Y.G.; Gong, T.; Huang, N.; Lv, X.W.; Fang, L.; Sun, X.H. Enhanced Oxygen Reduction and Evolution in N-Doped Carbon Anchored with Co Nanoparticles for Rechargeable Zn-Air Batteries. *Appl. Surf. Sci.* **2021**, *m*. [[CrossRef](#)]
39. Cheng, X.; Yang, J.; Yan, W.; Han, Y.; Qu, X.; Yin, S.; Chen, C.; Ji, R.; Li, Y.; Li, G.; et al. Nano-Geometric Deformation and Synergistic Co Nanoparticles-Co-N₄ Composite Sites for Proton Exchange Membrane Fuel Cells. *Energ. Environ. Sci.* **2021**, *14*, 5958–5967. [[CrossRef](#)]
40. Dai, Y.X.; Xin, W.L.; Xu, L.H.; Li, J.; Li, Y.X.; Li, J.; Cosnier, S.; Zhang, X.J.; Marks, R.S.; Shan, D. 2-Methylimidazole-tuned “4-Self” strategy based on benzimidazole-5-carboxylate for boosting oxygen reduction electrocatalysis. *Appl. Surf. Sci.* **2022**, *591*, 153066. [[CrossRef](#)]
41. Liu, T.; Zhao, S.; Wang, Y.; Yu, J.; Dai, Y.; Wang, J.; Sun, X.; Liu, K.; Ni, M. In Situ Anchoring Co-N-C Nanoparticles on Co₄N Nanosheets toward Ultrastable Flexible Self-Supported Bifunctional Oxygen Electrocatalyst Enables Recyclable Zn-Air Batteries Over 10000 Cycles and Fast Charging. *Small* **2022**, *18*, 2105887. [[CrossRef](#)] [[PubMed](#)]
42. Du, H.M.; Ding, F.F.; Gu, L.; Zhao, J.S.; Zhang, X.X.; Qu, K.G.; Li, Y.W.; Lan, T.Y.; Li, J.; Zhang, Y.; et al. CoO/Co/N-C Nanoparticles Embedded in Carbon as Mediate for Oxygen Reduction Electrocatalysts. *J. Alloy. Compd.* **2021**, *885*, 161174. [[CrossRef](#)]
43. Liang, Z.; Kong, N.; Yang, C.; Zhang, W.; Zheng, H.; Lin, H.; Cao, R. Highly Curved Nanostructure-Coated Co, N-Doped Carbon Materials for Oxygen Electrocatalysis. *Angew. Chem. Int. Ed.* **2021**, *60*, 12759–12764. [[CrossRef](#)] [[PubMed](#)]
44. Tan, M.Y.; Xiao, Y.Y.; Xi, W.H.; Lin, X.F.; Gao, B.F.; Chen, Y.L.; Zheng, Y.; Lin, B.Z. Cobalt-Nanoparticle Impregnated Nitrogen-Doped Porous Carbon Derived from Schiff-Base Polymer as Excellent Bifunctional Oxygen Electrocatalysts for Rechargeable Zinc-Air Batteries. *J. Power Sources* **2021**, *490*, 229570. [[CrossRef](#)]
45. Zhong, H.; Shi, C.; Li, J.; Yu, R.; Yu, Q.; Liu, H.; Yao, Y.; Wu, J.; Zhou, L.; Mai, L. Cobalt Decorated Nitrogen-Doped Carbon Bowls as Efficient Electrocatalysts for the Oxygen Reduction Reaction. *Chem. Commun.* **2020**, *56*, 4488–4491. [[CrossRef](#)] [[PubMed](#)]
46. Gao, J.; Hu, Y.; Wang, Y.; Lin, X.; Hu, K.; Lin, X.; Xie, G.; Liu, X.; Reddy, K.M.; Yuan, Q.; et al. MOF Structure Engineering to Synthesize CoNC Catalyst with Richer Accessible Active Sites for Enhanced Oxygen Reduction. *Small* **2021**, *17*, 2104684. [[CrossRef](#)]
47. Zhu, C.; Shi, Q.; Xu, B.Z.; Fu, S.; Wan, G.; Yang, C.; Yao, S.; Song, J.; Zhou, H.; Du, D.; et al. Hierarchically Porous M-N-C (M = Co and Fe) Single-Atom Electrocatalysts with Robust MN_x Active Moieties Enable Enhanced ORR Performance. *Adv. Energy Mater.* **2018**, *8*, 1801956. [[CrossRef](#)]
48. Leenders, S.H.; Becker, R.; Kumpulainen, T.; de Bruin, B.; Sawada, T.; Kato, T.; Fujita, M.; Reek, J.N. Selective Co-Encapsulation Inside an M₆L₄ Cage. *Chem. Eur. J.* **2016**, *22*, 15468–15474. [[CrossRef](#)]

49. Kawano, M.; Haneda, T.; Hashizume, D.; Izumi, F.; Fujita, M. A Selective Instant Synthesis of a Coordination Network and Its Ab Initio Powder Structure Determination. *Angew. Chem. Int. Ed.* **2008**, *47*, 1269–1271. [[CrossRef](#)]
50. Xiang, X.; Zhang, X.R.; Yan, B.W.; Wang, K.; Wang, Y.Q.; Lyu, D.D.; Xi, S.B.; Tian, Z.Q.; Shen, P.K. Atomic Iron Coordinated by Nitrogen Doped Carbon Nanoparticles Synthesized Via a Synchronous Complexation-Polymerization Strategy as Efficient Oxygen Reduction Reaction Electrocatalysts for Zinc-Air Battery and Fuel Cell Application. *Chem. Eng. J.* **2022**, *440*, 135721. [[CrossRef](#)]
51. Hong, Y.; Li, L.; Huang, B.; Tang, X.; Zhai, W.; Hu, T.; Yuan, K.; Chen, Y. Deciphering the Precursor–Performance Relationship of Single-Atom Iron Oxygen Electroreduction Catalysts via Isomer Engineering. *Small* **2022**, *18*, 2106122. [[CrossRef](#)] [[PubMed](#)]
52. Yang, Z.; Yan, X.; Tang, Z.; Peng, W.; Zhang, J.; Tong, Y.; Li, J.; Zhang, J. Facile Synthesis of Hemin-based Fe-N-C Catalyst by MgAl-LDH Confinement Effect for Oxygen Reduction Reaction. *Appl. Surf. Sci.* **2022**, *573*, 151505. [[CrossRef](#)]
53. Wan, X.H.; Guo, X.M.; Duan, M.T.; Shi, J.; Liu, S.J.; Zhang, J.H.; Liu, Y.J.; Zheng, X.J.; Kong, Q.H. Ultrafine CoO Nanoparticles and Co-N-C Lamellae Supported on Mesoporous Carbon for Efficient Electrocatalysis of Oxygen Reduction in Zinc-Air Batteries. *Electrochim. Acta* **2021**, *394*, 139135. [[CrossRef](#)]
54. Zhou, W.H.; Li, Y.; Zheng, L.C.; Liu, J.; Tang, R.R.; Shi, K.J.; Zhang, Y.Y. Three-Dimensional MOF-Derived Co and N Co-Doped Porous Carbon Bifunctional Catalyst for the Zn–Air Battery. *CrystEngComm* **2021**, *23*, 4930. [[CrossRef](#)]
55. Fu, Y.Y.; Xu, D.W.; Wang, Y.F.; Li, X.H.; Chen, Z.B.; Li, K.; Li, Z.F.; Zheng, L.R.; Zuo, X. Single Atoms Anchored on Cobalt-Based Catalysts Derived from Hydrogels Containing Phthalocyanine toward the Oxygen Reduction Reaction. *ACS Sustain. Chem. Eng.* **2020**, *8*, 8338–8347. [[CrossRef](#)]
56. Ha, Y.; Fei, B.; Yan, X.X.; Xu, H.B.; Chen, Z.L.; Shi, L.X.; Fu, M.S.; Xu, W.; Wu, R.B. Atomically Dispersed Co-Pyridinic N-C for Superior Oxygen Reduction Reaction. *Adv. Energy Mater.* **2020**, *10*, 2002592. [[CrossRef](#)]
57. Yi, J.D.; Xu, R.; Chai, G.L.; Zhang, T.; Zang, K.T.; Nan, B.; Lin, H.; Liang, Y.L.; Lv, J.Q.; Luo, J.; et al. Cobalt Single-Atoms Anchored on Porphyrinic Triazine-based Frameworks as Bifunctional Electrocatalysts for Oxygen Reduction and Hydrogen Evolution Reactions. *J Mater. Chem. A* **2019**, *7*, 1252–1259. [[CrossRef](#)]
58. Zhang, M.; Dai, Q.; Zheng, H.; Chen, M.; Dai, L. Novel MOF-Derived Co@N-C Bifunctional Catalysts for Highly Efficient Zn-Air Batteries and Water Splitting. *Adv. Mater.* **2018**, *30*, 1705431. [[CrossRef](#)]